RSC Advances

PAPER

View Article Online
View Journal | View Issue



Cite this: *RSC Adv.*, 2026, **16**, 25865

# First-principles study of $ALiZnS_2$ (A = Na, Rb) promising quaternary chalcogenides for energy harvesting

Muhammad Salman Khan, *[a] Mohannad Al-Hmoud,[b] Banat Gul,[c] Ayed M. Binzowaimil,[b] Ghlamallah Benabdellah,[d] Zia Ullah,[e] Hijaz Ahmad[f] and Ahmad Irfan[g]

First-principles calculation is employed to explore the structural, elastic, optoelectronic and transport features of novel $ALiZnS_2$ (A = Na, Rb) quaternary chalcogenides. The Rb-based material has a greater equilibrium volume and compressibility. Elastic constant calculation confirms Born stability for both materials. $NaLiZnS_2$ has larger bulk (44 GPa), shear (25 GPa), and Young's (67 GPa) moduli, demonstrating improved stiffness, while $RbLiZnS_2$ shows improved ductility with a higher Pugh ratio (1.68) and stronger ionic character, as reflected by its larger positive Cauchy pressure. Direct wide energy gaps of 3.43 eV ($NaLiZnS_2$) and 4.04 eV ($RbLiZnS_2$) are found (with TB-mBJ) with S-p states dominating the valence band, and Zn-s/p states controlling the conduction band region. Replacement of Rb widens the conduction band and enhances the separation of ions. The optical spectra indicate that $NaLiZnS_2$ has extensive dielectric peaks, a higher refractive index (~2.8), improved UV absorption and a high plasma frequency (~18 eV) as compared to $RbLiZnS_2$. In the study of thermoelectric transport nature, the electrical conductivity and Seebeck coefficient decrease with temperature, lattice thermal conductivity is suppressed by Umklapp scattering, and $NaLiZnS_2$ ($ZT$ = 0.46) shows a maximal figure of merit compared to $RbLiZnS_2$ ($ZT$ = 0.38). The results confirm $MLiZnS_2$ materials as mechanically stable, optically transparent UV materials with potential mid-temperature thermoelectric potential, and adjustable through alkali-metal substitution.

Received 8th March 2026
Accepted 11th May 2026

DOI: 10.1039/d6ra01982j

rsc.li/rsc-advances



## 1 Introduction

Multinary metal sulfides are becoming increasingly popular due to their various structural variants[1–3] and exceptional physicochemical properties.[4–6] Multinary sulfides containing transition metals are especially intriguing because they usually exhibit several coordination modes with $S_2$.[7,8] The diversity of structural units and the way they aggregate are the major reasons for materials' complex structures, which have a direct impact on their properties and applications.[9] Transition metal chalcogenides with alkali-substitutes have received considerable interest after the proposal of the $A_xFe_{2-y}Se_2$ (A = Na, K, Rb, Cs) superconductors, which have superconducting transition temperatures of as high as approximately 30 K.[10,11] To balance the charge, it is common to have vacancies in both the alkali and transition metal sites, and these defects tend to have a final say on the crystal structures and physical properties, as seen in the aforementioned two types of structures.[12] Similarly, $A_xFe_{2-y}S_2$ does not exhibit superconductivity, presumably due to the existence of iron vacancies, but tetragonal FeS, having no vacancies, is superconducting at temperatures of about 5 K.[13,14] Further, the transition metal site can be readily replaced by monovalent cations, like $Cu^+$, $Ag^+$, and $Li^+$, to produce vacancy-free analogues.[15,16] Quaternary sulfide created by the insertion of alkali ions into chalcopyrite has been recognized as a potential intercalation cathode.[17] The $LiCuFeS_2$ is a single such cathode material proposed as a high-temperature secondary lithium battery cathode.[18] The alkali metal ions are incorporated in the 3D chalcopyrite structure in these compounds and form distinctive quaternary layered sulfides $MCuFeS_2$ (M = Li, Na, K, Rb, Cs).[19] Arrangement of sulfur anions, Cu and Fe cations occurs in hollow tetrahedral spaces created by the hexagonal dense packing of sulphur bent structures.[20] Quaternary sulfide

[a]*Department of Physics, Abdul Wali Khan University, Mardan, 23200, Pakistan. E-mail: salmankhan73030@gmail.com*
[b]*Department of Physics, College of Science, Imam Mohammad Ibn Saud Islamic University (IMSIU), Riyadh, 13318, Saudi Arabia*
[c]*National University of Sciences and Technology (NUST), Islamabad, Pakistan*
[d]*Laboratory of Physical Engineering, Department of Physics, Faculty of Matter Sciences, University of Tiaret, Algeria*
[e]*Key Laboratory of Materials Physics, Ministry of Education, School of Physics, Zhengzhou University, Zhengzhou 450052, P. R. China*
[f]*Irfan Suat Gunsel Operational Research Institute, Near East University, Nicosia/TRNC, 99138 Mersin 10, Turkey*
[g]*Department of Chemistry, College of Science, King Khalid University, P.O. Box 9004, Abha, 61413, Saudi Arabia*

materials based on $ACuMS_2$ (where A = alkali metal and M = 3d transition metals) were just studied for their electrical transport behaviour in $ACuFeS_2$ (where A = K, Rb, Cs), including the electrical conductivity and resistivity characteristics.[21] This work carried out the synthesis of a novel group of quaternary sulfides, $ACuMS_2$ (A K, Rb, Cs; M Mn, Co),[22] that crystallize with the $ThCr_2Si_2$-type structure. The positive growth of the $ACuMS_2$ phases (A = K, Rb, Cs; M = Mn, Co, Fe), and the presence of the $NaCuFeS_2$ phase indicate that substitution of Fe in $NaCuFeS_2$ with Mn or Co would lead to new compounds, *i.e.* $NaCuMnS_2$ and $NaCuCoS_2$. Kacholovskaya *et al.*[23] discovered another quaternary sulfide, $NaCuZnS_2$, by identifying the mineral chvilevait as having a composition of $Na(Cu, Fe, Zn)_2S_2$. Structurally, cubic ZnS and $CuFeS_2$ chalcopyrite are closely linked since the latter may be considered the zinc blende superstructure in which the atoms of Cu and Fe are equally distributed.

Oledzka *et al.*[24] prepared four different low-dimensional $NaCuAS_2$ (A = Mn, Co, Fe, and Zn) quaternary sulfides. Virtue *et al.*[25] produced $KCuMnS_2$ and $KLiMnS_2$ *via* a high-temperature reaction of K and Li carbonates with pure metals in a $CS_2$. Predictions of theoretical studies have led to the discovery of a novel family of two-dimensional quantum spin Hall (QSH) insulators in transition-metal halide monolayers, marking one of the first instances of QSH-based halide materials.[27] Similarly, *ab initio* studies have suggested quantum anomalous Hall insulating states in Sn–Ge honeycomb lattices with significant energy gaps of 0.34 eV and 0.06 eV, respectively, which could be beneficial for applications at room temperature.[28] It is evident that small adjustments in lattice symmetries and element compositions can significantly impact the electronic and transport characteristics of materials. Experimental studies have focused on synthesizing novel compounds, including crystal structure analysis and disordering effects, as well as structural parameter redetermination to increase reliability and reproducibility.[29] Liu *et al.*[30] synthesized and successfully investigated two new quaternary layered materials, $NaLiFeS_2$ and $NaLiCoS_2$, as well as $NaLiMnS_2$, utilizing powder X-ray diffraction, magnetic, electrical resistivity, and optical investigations. The discovery of the effect that excess S has on the rate of the formation of quaternary sulfide minerals from the application of late transition metals has created a significant step forward in the ability to produce these types of materials.[31] The current research contributes to such initiatives through first-principles calculations for the purpose of investigating the structural stability and multifunctionalities of $NaLiZnS_2$ and $RbLiZnS_2$ chalcogenides, which are not yet experimentally synthesized. A comprehensive evaluation was carried out of the multifaceted properties of these new materials, showing the significant relationships that exist between their structure and properties, along with how the substitution of different alkali metals changes the stability of the lattice, the bonding character and how the materials conduct electrons. This understanding is critical in identifying these materials as possible candidates for optoelectronic devices, thermoelectric use, and energy-harvesting technology. Not only does this research add to the theoretical library of quaternary sulfides, but it also provides early guidance on effective synthesis and material optimization in the future.

## 2 Computational details

Electronic structure calculations were carried out with the density functional theory (DFT) and two distinct exchange–correlation functionals: the Wu–Cohen generalized gradient approximation (WC-GGA)[32] and the Tran–Blaha modified Becke–Johnson potential (TB-mBJ).[33] To obtain structural precision and enhance band gap prediction, both electronic structure calculations were performed using the density functional theory (DFT) and two different exchange–correlation schemes: the Wu–Cohen generalized gradient approximation (WC-GGA) and the Tran–Blaha modified Becke–Johnson. WC-GGA is an effective option in the geometry optimization step since it can produce structural parameters that are of much more consistent qualification with experimental measurements and minimises systematic errors in further electronic structure research. The TB-mBJ potential have been employed, which is a semi-local exchange potential that was developed by Tran and Blaha to improve the band gap predictions without drawing heavy computing expenses as in many-body perturbation methods like GW. The computational procedure needed initial structural optimization using WC-GGA until all atoms' stresses were less than a preset threshold ($10^{-4}$ Ry per Bohr) and the overall energy change was less than $10^{-6}$ Ry. A full-potential all-electron approach, employed in the WIEN2K software,[34] was used to address the core and valence states without shape approximations for the potential and charge density. The muffin-tin radii (RMT) of each atomic species were optimally selected so as to be non-overlapping and to maximize the quality of the basis set, and the plane-wave cutoff was adjusted by the parameter RMT $\times$ $K_{max}$ (which is commonly set to 7.0–9.0) in order to provide convergence. A high-density Monkhorst–Pack *k*-point grid (*e.g.* 10 $\times$ 10 $\times$ 10) was used to sample the Brillouin zone, case giving total energy convergence of 1 meV per atom. To ensure that the same structural parameters were used and to minimize any possible discrepancies, a self-consistent field (SCF) calculation was performed with TB-mBJ after optimizing the lattice parameters employing WC-GGA to calculate the electronic features. A balanced approach is achieved when WC-GGA is used to obtain the structure, and TB-mBJ is used to obtain the electrical properties. WC-GGA cures the lattice constant exaggeration found in PBE, but TB-mBJ produces band gaps and optical spectra that are highly accurate compared to experimentally measured values across a large range of semiconductors and insulators. The resulting combination of this type of approach guarantees that the calculated band dispersions, effective masses, and DOS features capture a correct underlying crystal geometry and an exchange–correlation potential that captures properly the effects of electronic localization, which are relevant to gap formation, leading to an extensively used methodology in computational materials science.

## 3 Results and discussions

### 3.1 Structural properties

$NaLiZnS_2$ is found in the tetragonal $I4m2$ space group (see Fig. 1). $Na^{1+}$ was coupled with the six $S^{2-}$ atoms to produce $NaS_6$ octahedra, which have six similar $LiS_4$ tetrahedra, six similar $ZnS_4$

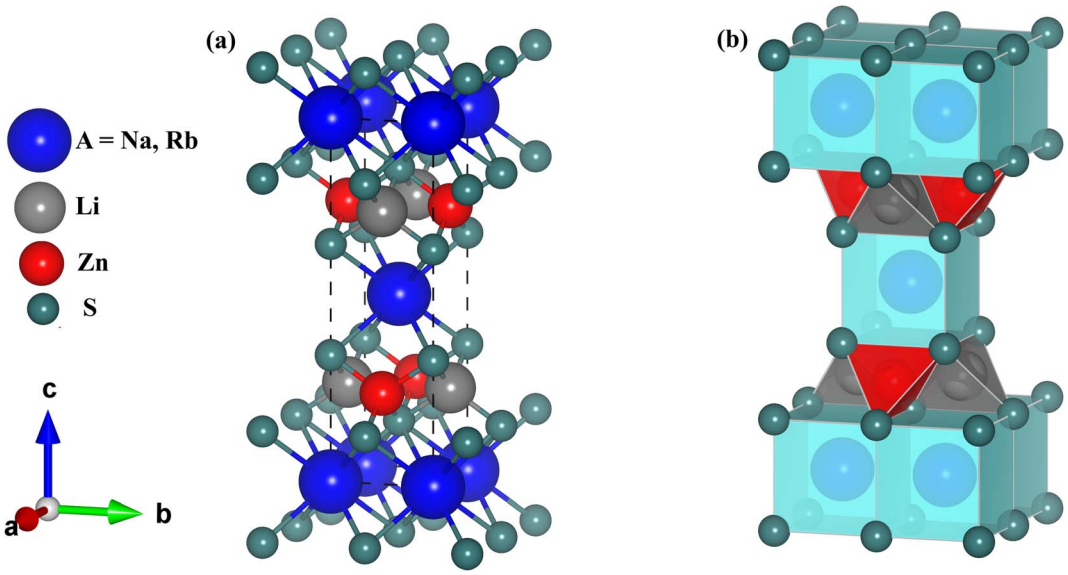


Fig. 1 The computed (a) unit cell crystal structure and (b) polyhedral representation of $ALiZnS_2$ (A = Na, Rb) quaternary chalcogenides.

tetrahedra, and six similar $LiS_4$ tetrahedra and three similar $ZnS_4$ tetrahedra. The length of Na–S bonds ranges between 2.84 Å and 3.04 Å. The $Li^{1+}$ connection with four $S^{2-}$ atoms generates $LiS_4$ tetrahedra, but its corners are shared by six identical $NaS_6$ octahedra, four similar $LiS_4$ tetrahedra, three of its $NaS_6$ octahedra, and three identical $ZnS_4$ tetrahedra. Angles of corner-sharing octahedra tilt range from 21 to 54°. One of these is a smaller (2.32 Å) Zn–S bond, while the other three are larger (2.45 Å). The two sites for $S^{2-}$ are incompatible. The initial $S^{2-}$ site forms 7-coordinate connections with three equivalent $Na^{1-}$ atoms, one $Li^{1-}$ atom, and three equivalent $Zn^{2-}$ atoms. The $S^{2-}$ site $S^{2-}$ contains three equivalent and equivalent $Na^{+}$, three equivalent $Li^{+}$, and a single $Zn^{+}$ atom, respectively. $RbLiZnS_2$ is a product of alpha bismuth trifluoride, and its crystal structure is tetragonal *I*4*m*2. $Rb^{1+}$ takes the form of an eight-fold body-centred cubic structure with eight linked $S^{2-}$ atoms. Each Rb–S bond measures 3.54 Å. Four similar $S^{2-}$ atoms are joined to $Li^{1+}$ to produce $LiS_4$ tetrahedra. The sides and edges of these tetrahedra will connect four more tetrahedra of $ZnS_4$ and four more tetrahedra of $LiS_4$. All Zn–S bonds measure 2.42 Å. $S^{2-}$ is coordinated in an 8-coordination geometry with four similar $Rb^{1+}$, two similar $Li^{1+}$, and two similar $Zn^{2+}$. Lattice parameter values (see Table 1) for $NaLiZnS_2$ and $RbLiZnS_2$ were found to be in close conformity with previous findings[17,26,30,31] with slight deviations and confirming the accuracy of the optimized lattice structure.

Fig. 2(a and b) displays the change of total energy as a function of unit cell volume for $NaLiZnS_2$ and $RbLiZnS_2$, demonstrating the equation of state behaviour derived from first-principles calculations. Both curves show a parabolic Murnaghan-type relationship. The curves in both materials are symmetric around the minimum, indicating an isotropic elastic response near equilibrium. The sharp increase in energy of volumes larger or smaller than $V_0$ suggests this is the high repulsive or tensile force related to compression or expansion of lattices. $NaLiZnS_2$ possesses a slightly lesser equilibrium volume than $RbLiZnS_2$ because $Na^{+1}$ has a smaller ionic radius, thus forming a compact lattice structure. The radius of curvature of the $NaLiZnS_2$ plot around the minimum is slightly stiffer, and this is characteristic of denser structures with shorter bond lengths. The larger $RbLiZnS_2$ also has a larger equilibrium volume and is a slightly flatter source of curvature near the minimum. This means that it is more compressible and its bulk modulus is lower. The absolute total energies vary widely in magnitude in response to variations in atomic composition and mass, but in comparing the relative stability at constant chemical family, the relative location of the minimum in the volume axis is of more physical significance than the direct energies. The shape of the two curves is parabolic, which confirms that both materials are mechanically stable at their respective equilibrium states, as confirmed by the fact that the second derivative of energy *versus* volume is positive. Besides, the larger equilibrium volume of the $RbLiZnS_2$ can affect its density, phonon dispersion and ultimately its thermal and thermoelectric characteristics. This might result in lower lattice thermal conductivity with increased phonon scattering in the more open structure. The denser $NaLiZnS_2$ structure may have greater sound velocities and heat conductivity, but it is also more rigid. Calculation of cohesive energy ($E_{coh}$) and formation energy ($E_{form}$) is essential for understanding the thermodynamic stability and atomic interactions in $NaLiZnS_2$ and $RbLiZnS_2$. Both materials exhibit relatively high cohesive energy: −4.43 eV per atom for $NaLiZnS_2$ and −4.32 eV per atom for $RbLiZnS_2$. High cohesive energy implies that $NaLiZnS_2$ and $RbLiZnS_2$ demonstrate strong atom-to-atom interaction in their crystalline structures. Cohesive energy is defined as the energy necessary to separate molecules or ions into individual atoms, meaning that lower energy values indicate a more stable material structure. Thus, since the cohesive energy of $NaLiZnS_2$ is more negative than that of $RbLiZnS_2$, it can be concluded that this compound demonstrates stronger bonding and a more

Table 1 The lattice constants, cohesive energies, band gaps (TB-mBJ), and formation energies for $ALiZnS_2$ (A = Na, Rb) quaternary materials

| Materials | $a$ (Å) | $b$ (Å) | $c$ (Å) | $E_{coh}$ (eV per atom) | $E_g$ (eV) | $E_{form}$ (eV per f.u) |
|---|---|---|---|---|---|---|
| $NaLiZnS_2$ (our work) | 3.98 | 3.98 | 6.69 | −4.43 | 3.43 | −4.17 |
| $RbLiZnS_2$ (our work) | 4.06 | 4.06 | 13.79 | −4.32 | 4.04 | −4.13 |
| $RbLiZnS_2$ | 4.02[a] | | 13.76[a] | | 3.55[a] | −4.18[a] |
| $CsLiZnS_2$ | 4.08[a] | | 14.28[a] | | 3.61[a] | −4.18[a] |
| $KLiZnS_2$ | 3.97[a] | | 13.37[a] | | 3.58[a] | −4.20[a] |
| $NaLiMnS_2$ | 4.04[b] | | 6.72[b] | | 2.80[b] | |
| $NaLiCoS_2$ | 3.95[b] | | 6.70[b] | | 1.50[b] | |
| $KAgCdS_2$ | 4.27[c] | | 7.67[c] | | 1.92[c] | |
| $RbAgCdS_2$ | 4.25[c] | | 13.90[c] | | 2.16[c] | |
| $CsAgCdS_2$ | 4.31[c] | | 14.26[c] | | 2.42[c] | |
| $NaLiCdS_2$ | 4.13[d] | | 6.86[d] | | 2.40[d] | |
| $NaLiZnS_2$ | 3.97[d] | | 6.71[d] | | 2.37[d] | |

[a] Ref. 17. [b] Ref. 26. [c] Ref. 30. [d] Ref. 31.

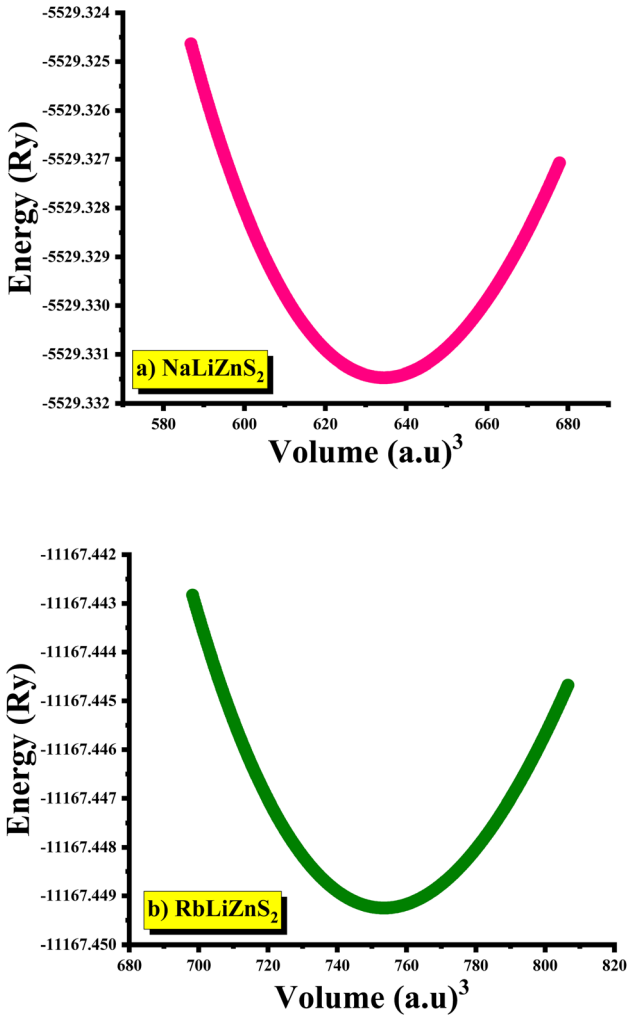


Fig. 2 The optimization curves of (a) $NaLiZnS_2$ and (b) $RbLiZnS_2$ quaternary materials.

stable lattice than $RbLiZnS_2$ due to the smaller size of $Na^+$ ions, contributing to more significant orbital overlapping. Likewise, the formation energies of −4.17 eV per f.u for $NaLiZnS_2$ and −4.13 eV per f.u for $RbLiZnS_2$ (see Table 1) are also highly negative, proving the stability of these compounds with respect to their constituent elements. Formation energy is the energy released during the formation reaction when a compound is formed from its elemental reference state; hence, any negative value shows that the formation reaction is exothermic. Formation energy values obtained during the study were found to have a high correlation with the theoretical values from the literature, thus validating the stability trends reported by previous studies.[17,26,30,31] In comparison, the marginally more negative $E_{form}$ for $NaLiZnS_2$ shows a greater stability level than the other compound. The close values, however, show that although both compounds are stable, substituting Na with Rb makes the structure less stable due to the expansion of the crystal lattice and weak bonding interactions. Considering the similarities between trends for cohesive and formation energy, both compounds can be concluded to be inherently stable. However, $NaLiZnS_2$ shows greater stability due to stronger bonding energy, which agrees with its mechanical properties shown in the elastic properties analysis.

### 3.2 Mechanical properties

The elastic behaviour of $NaLiZnS_2$ and $RbLiZnS_2$ is studied exclusively in a physically transparent and logically correlated manner with their mechanical, bonding and anisotropic behaviour, a critical consideration when determining whether to utilize them as stable semiconductor materials. The validation of all Born–Huang stability conditions for tetragonal systems: $C_{11} > |C_{12}|$, $C_{33} > 0$, $C_{44} > 0$, $C_{66} > 0$, and $2C_{13} < C_{33}(C_{11} + C_{12})$ confirm their mechanical stability. $NaLiZnS_2$ with 44 GPa and $RbLiZnS_2$ with 40 GPa have a relatively small bulk modulus (see Table 2), suggesting a moderate ability to sustain uniform volumetric compression; this is normal in semiconductor materials, in which ionic bonding is the predominant type of bonding. Bulk modulus values computed were found to be comparable with reported values for other quaternary sulfides, thus validating the consistency in resistance to compression.[17] $NaLiZnS_2$ boasts of a high bulk modulus, indicating a well-bonded material that is not easily compressible. This is

Table 2 The calculated elastic coefficients, elastic moduli, Bulk Modulus ($B$), Cauchy pressure ($C''$), Young Modulus ($Y$), Shear Constant ($C'$), Shear Modulus ($G$), Poisson's ratio ($\nu$), Pugh-ratio, and Anisotropy constant ($A$) of the $ALiZnS_2$ (A = Na, Rb) quaternary materials

| Materials | $C_{11}$ | $C_{12}$ | $C_{13}$ | $C_{33}$ | $C_{44}$ | $C_{66}$ | $B$ | $C''$ | $Y$ | $C'$ | $G$ | $\nu$ | $B/G$ | $A$ |
|---|---|---|---|---|---|---|---|---|---|---|---|---|---|---|
| $NaLiZnS_2$ (our work) | 91 | 36 | 20 | 73 | 23 | 31 | 44 | 13 | 67 | 27 | 25 | 0.24 | 1.65 | 1.13 |
| $RbLiZnS_2$ (our work) | 78 | 29 | 19 | 77 | 22 | 24 | 40 | 7 | 59 | 24 | 24 | 0.25 | 1.68 | 0.99 |
| $NaLiZnS_2$ | 88[a] | 31[a] | 17[a] | 67[a] | 18[a] | 27[a] | 40[a] | | 58[a] | | 23[a] | | | |
| $RbLiZnS_2$ | 74[a] | 22[a] | 16[a] | 73[a] | 21[a] | 21[a] | 35[a] | | 51[a] | | 22[a] | | | |
| $CsLiZnS_2$ | 69[a] | 22[a] | 17[a] | 82[a] | 22[a] | 21[a] | 35[a] | | 54[a] | | 22[a] | | | |
| $KLiZnS_2$ | 79[a] | 24[a] | 16[a] | 68[a] | 21[a] | 23[a] | 35[a] | | 56[a] | | 22[a] | | | |

[a] Ref. 17.

because $Na^+$ possesses a low ionic radius and a high electrostatic field as compared to those of $Rb^+$. Substitution of Na with heavier and electropositive Rb causes the bond lengths to increase, the charge density to decrease, and the interatomic forces to become less strong, decreasing the resistance to hydrostatic pressure. The direction of this trend is absolutely in line with chemical perception, and this is a good basis on which to explain the rest of the stretch properties. $NaLiZnS_2$ has a shear modulus ($G$) of 25 GPa, with $RbLiZnS_2$ having 24 GPa (see Table 2). It means that $NaLiZnS_2$ is stiffer. The calculated values for the shear modulus show high correspondence with previous reports,[17] confirming their mechanical properties and rigidity. The presence of Na makes $NaLiZnS_2$ have a higher shear modulus, stronger directional bonding and a more rigid Zn–S frame, as well as shear deformation is not only related to compression. The structure of $RbLiZnS_2$ is more flexible with a lower shear modulus because the contacts between Rb and S are weaker, and also because it is more ionic. This renders shear distortion under tension very much easier. The values of the Young's modulus ($Y$) estimated as 67 GPa for $NaLiZnS_2$ and 59 GPa for $RbLiZnS_2$ (see Table 2) were the mechanical strength of the Na-based material during uniaxial loading. Young's modulus values estimated were found to correlate well with literature values,[17] thus confirming similar stiffness values and structural stability. $NaLiZnS_2$ is less inclined to the plastic process of elongation or compression in specific dimensions since it takes more load on a higher Young's modulus to generate such an elastic strain. $RbLiZnS_2$ has a lower Young's modulus, and this could be helpful in compliance and preventing strain-induced flaws during growth or thermal cycling. Materials with higher Young's modulus are more consistent during the manufacturing and operation of devices. $NaLiZnS_2$ and $RbLiZnS_2$ have Poisson ratios ($\nu$) of 0.24 and 0.25, respectively, which provide important data regarding interatomic bonds and processes of deformation. These values fall in the scale of materials with mixed ionic-covalent bonding, indicating that neither of the two compounds is covalent or ionic. The Poisson ratio of $RbLiZnS_2$ is a little higher, meaning that it is more laterally sensitive to uniaxial stress than other, less strongly directional-bonded materials. $NaLiZnS_2$ possesses a lower value, and this indicates that it will make it resistant to transverse deformation because of its more rigid bonding networks. This is then followed by the reasoning to the Cauchy pressure ($C_s$), and $C_{12} - C_{44}$ and is bonding in nature. The positive values recorded 13 GPa and 7 GPa for the case of $NaLiZnS_2$ and $RbLiZnS_2$, respectively, are a clear indication of the ionic bonding contribution within each material.

Non-directional bonding contacts are common in positive Cauchy pressure, and high covalent directionality is indicated by negative values. Positive values of Cauchy pressure determined were found to correlate well with previous studies,[17] thus confirming the ionic nature of the bonding between constituent atoms. $RbLiZnS_2$ has positive Cauchy pressure due to the fact that its Rb atom is electropositive, which means that it will rearrange faster when subjected to stress. The small but positive value of $NaLiZnS_2$ is a sign of the balanced ionic-covalent interaction, which leads to increased stiffness and reduced ductility. The second item in the table is the Pugh ratio ($B/G$), which is an empirical statistic of ductility/brittleness, much used. The calculated values of both ratios (see Table 2) of $NaLiZnS_2$: 1.65 and $RbLiZnS_2$: 1.68 bring both the materials near the pivotal value of 1.66 that distinguishes between ductile and brittle behaviour. These findings prove that $NaLiZnS_2$ is brittle and has a lower $B/G$ ratio and directional bonding, and $RbLiZnS_2$ is ductile and has a higher $B/G$ ratio and softer lattice. This difference is critical in practice as the ductile materials are less vulnerable to mechanical stress and microcrack propagation as compared to the brittle ones, which are stiffer and resistant to thermal change. The shear constant $(C_{11} - C_{12})/2$ presented (see Table 2) is similar to 27 GPa ($NaLiZnS_2$) and 24 GPa ($RbLiZnS_2$). It possesses tetragonal shearing deformation strength. The calculated values for the shear constant have high correspondence with previous reports,[17] indicating that they exhibit comparable resistance to shear deformation. A large $C$ exhibits a tremendous resistance to distortions that lead to the impairment of symmetry, which is essential in ensuring structural integrity under complicated stress. $NaLiZnS_2$ possesses a significantly higher value of $C$, which means it is less prone to lattice destabilization and is shear-rigid. $RbLiZnS_2$ has a lower value, and this demonstrates that it enhances shear compliance and offers a more ionic, softer bonding environment. The quantitative outcome A is given by the ratio of $2C_{44}/C_{11} - C_{12}$, and the values of anisotropy of elasticity are 1.13 ($NaLiZnS_2$) and 0.99 ($RbLiZnS_2$). Such a difference in unity values indicates direction-dependent elastic behaviour, an inherent characteristic of tetragonal crystal structures because of their natural structure anisotropy. The medium separation between the two materials indicates the moderate divergence of unity, indicating that

although the elastic properties depend on the crystallographic direction, anisotropy is not too high and leads to a mechanically stable and predictive behaviour. Anisotropy is marginally smaller in $RbLiZnS_2$, and the ionic bonding is weaker and more isotropic, giving it a more homogenous elastic response. The pattern of all the elasticity parameters in the table is consistent and quite intuitive: not only is $NaLiZnS_2$ mechanically stronger, but it is also less compressible and more brittle, which has stronger and more directional bonds, whereas $RbLiZnS_2$ is not only softer, but also more compressible, more indicative of ductile behaviour, and more ionic. This developmental history of elastic behaviour highlights both the applicability of substitution of alkali-metals in defining the mechanical behaviour of sulfide semiconductors, as well as provides a basis to attribute mechanical stability to electronic and functional activity in sulfide semiconductors.

### 3.3 Electronic properties

Two exchange–correlation models were used to estimate the electronic band structure of both $NaLiZnS_2$ and $RbLiZnS_2$ quaternary chalcogenides: the Wu–Cohen generalized gradient approximation (WC-GGA) and the Tran–Blaha modified Becke–Johnson potential (TB-mBJ) (Fig. 3(a and b)). WC-GGA foresees a band gap of 1.80 eV of $NaLiZnS_2$; TB-mBJ increases it much more, to 3.43 eV. Band gaps estimated using TB-mBJ in the current study showed a correlation with reported values from the literature, which confirms the accuracy of the exchange–correlation method utilized in the studies.[17,26,30,31] WC-GGA gives a band gap of 2.43 eV in $RbLiZnS_2$, and TB-mBJ gives it a 4.04 eV band gap. This vast gap expansion over TB-mBJ is familiar with the fact that standard GGA methods contain inherent underestimation of band gaps because of errors of self-interaction and absence of proper derivative discontinuity in the exchange–correlation potential, and TB-mBJ, being a semi-local potential, is specifically designed to make better band gap predictions by better approximating the exchange potential, which increases conduction bands over GGA. $RbLiZnS_2$ has a higher band gap than $NaLiZnS_2$ (by 0.67 eV at WC-GGA and 0.52 eV at TB-mBJ), which means that its ionic bonding is more intense, and the energy barriers between valence and conduction are larger. This may be explained by the fact that $Rb^{+1}$ has a larger ionic radius, and this influences bond lengths, orbital overlaps and consequently electronic dispersion. Conduction bands of the two materials exhibit a small dispersion, meaning that electron mass can be relatively low, which can enhance carrier mobility, which is significant in thermoelectric and optoelectronic applications. The CBM and VBM coincide at the same locations of the Brillouin zone because of the existence of a direct energy gap in both materials. Flatter band features, especially on the valence side, may also provide significant contributions to high Seebeck coefficients because of a state density increase around the Fermi level. $NaLiZnS_2$ is a narrow to medium band gap semiconductor, potentially operational in the visible spectrum, under WC-GGA, with $RbLiZnS_2$ already approaching the wide-band-gap space, as per the gap values. Since $RbLiZnS_2$ (4.04 eV) has higher breakdown voltages than $NaLiZnS_2$ (3.57 eV), $RbLiZnS_2$ is more appropriate for near-UV, while $NaLiZnS_2$ (3.57 eV) can be used in deep-UV optoelectronic devices and high-power electronics. This also affects their optical absorption boundaries and transparency windows, with the larger the gaps, the more optical transparency in the visible and the less solar spectrum is used in photovoltaic applications.[35] However, the substitution of Na with the bigger, heavier Rb atom results in subtle differences. Materials have an S-p dominance of the VBM in the range of 5 eV to 0 eV, which is a strong indication of delocalization and hybridization of the states with Zn. This strengthens covalent Zn–S. Below this −6 eV to −5 eV, Zn-d orbitals exhibit sharp and narrow peaks, indicating their confined nature and insignificant dispersion, which contribute to deep valence states. Na-p orbital peaks in $NaLiZnS_2$ overlap between −4 eV and −1 eV in the S-p, which means weak hybridization and insignificant participation in the bonding. $RbLiZnS_2$ has sharper and stronger Zn-d peaks outside 6 eV, possibly because Rb causes lattice expansion that affects the symmetry of the Zn–S bonds and increases the localization of d-states. Nevertheless, in the VBM, the S-p dominance is present. In $NaLiZnS_2$, the conduction band starts right above 2 eV and is mainly generated by Zn-s and Zn-p states, whereas in $RbLiZnS_2$, Rb-s, Rb-p, and most importantly, spatially extended Rb-d ($n = 4$) states (also) come into play at much higher energies. This results in a larger, more dense CB profile, which can enhance electronic conduction in the doped or laser-doped case by offering more ready states to scatter the carriers in higher-energy channels. The effective masses of the charge carriers at CBM and VBM can be qualitatively determined from the curvature of band structures, as a greater curvature corresponds to a smaller effective mass and hence greater carrier mobility. With respect to TB-mBJ, the value of $m_e^* = 0.23\ m_o$ for $NaLiZnS_2$, whereas it is $m_e^* = 0.19\ m_o$ for $RbLiZnS_2$. As for the effective hole mass, it is found that the $m_h^* = 0.68\ m_o$ for $NaLiZnS_2$ and $m_h^* = 0.55\ m_o$ for $RbLiZnS_2$. Both $NaLiZnS_2$ and $RbLiZnS_2$ have dispersive conduction bands close to CBM, specifically in TB-mBJ calculations, revealing smaller electron effective masses. The curvature of the CBM of $NaLiZnS_2$ is high, leading to the low effective mass of electrons ($m_e^* \approx 0.23\ m_o$) and thus favouring high electron mobility. In comparison, the CBM region of $RbLiZnS_2$ demonstrates a similar dispersion of the conduction bands; however, due to a larger atomic radius of Rb, it has a slightly higher curvature than $NaLiZnS_2$, leading to the slightly higher electron effective mass. On the other hand, both compounds show rather flat valence bands at VBM, with a particularly high curvature in $NaLiZnS_2$, pointing to relatively large hole effective masses ($m_h^* \approx 0.55\ m_o$). As can be seen, hole mobility is significantly lower compared to that of electrons. It can be noted that $RbLiZnS_2$ exhibits slightly greater dispersion around the VBM compared to $NaLiZnS_2$, which suggests slightly smaller hole effective mass and, therefore, better hole transport. It is evident that the differences between electron and hole effective masses reflect the built-in asymmetry of carrier mobility; electrons are more efficient conductors of electric current. All of these results are validated by the analysis of the density of states and contribution of particular orbitals;

 

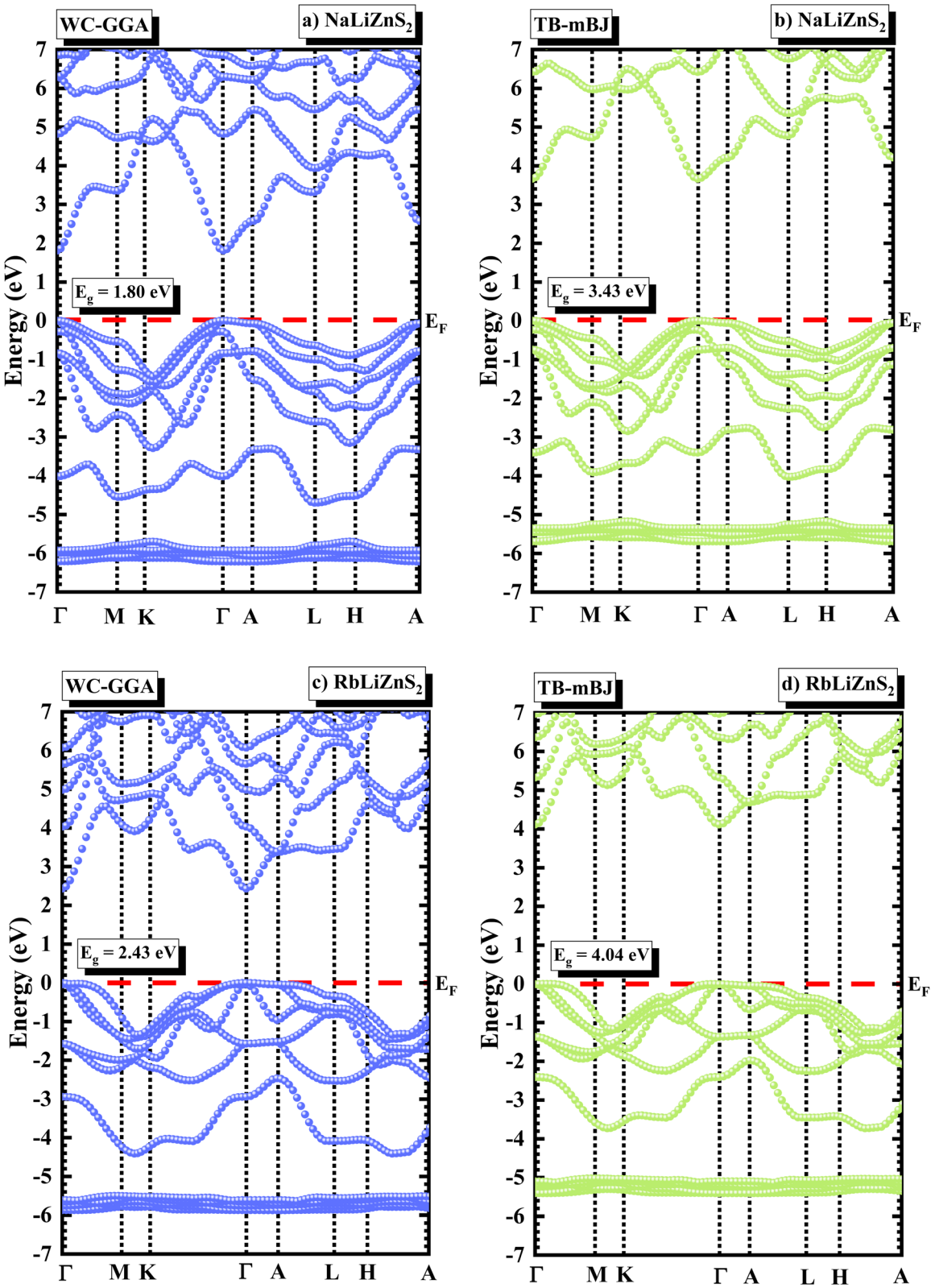


Fig. 3 The band structures for (a and b) $NaLiZnS_2$ and (c and d) $RbLiZnS_2$ materials using WC-GGA and TB-mBJ potentials.

it is clear that Zn-s/p bands contribute to the formation of dispersive conduction bands, whereas S-p bands contribute to the formation of flat valence bands. Both materials have favourable electronic properties for electron transport due to small electron effective masses, while large hole effective masses promote high Seebeck coefficients.

The S-p orbitals with energies from −5 to 0 eV are the major constituents of the valence band maximum (VBM) of $NaLiZnS_2$. Such huge and strong PDOS peaks (see Fig. 4) indicate the delocalization of the S-p electrons as well as the high hybridization of the electrons with atoms around it, especially Zn. The S–s orbitals are also less active and the ones confined to low energies, −5 to −3 eV, meaning that they are more isolated and less active in the covalent bonding at the Fermi level. The deep valence range of −6 eV to −5 eV has narrow and high peaks due to the Zn-d orbitals. It demonstrates that localized electronic states, as desired by transition metal d-orbitals, are not strongly hybridized with other orbitals but contribute to the enhancement of the density of states in the lower VB. Na-p orbitals hybridize with S-p orbitals between −4 eV and −1 eV and show weak hybridization and no participation in bonding. Na-s states, on the other hand, are nearly non-existent in the valence region and only become dominant above 5 eV in the conduction band, indicating an ionic nature and lack of binding to the Fermi level. Due to the high electron positivity of lithium and the small size, the Li-s orbital exhibits small, narrow peaks just below the Fermi level and once higher than 2 eV in the CB, suggesting minimal hybridization and bonding. The Zn-s and Zn-p states shape the conduction band of $NaLiZnS_2$, which has its onset at 2 eV but goes above 6 eV. These orbitals influence the curvature of the electron bands, the mass of the electrons, and consequently, the electrical conductivity of the substance. This region can have the contribution of minor contributions from the Na-s/p orbitals, but they are minimal. The empty orbitals that make up the Na states in the conduction band are only important at high energies and give insignificant contributions in the vicinity of the edges of the band. The carrier density of the material is low in the intrinsic state. The same can be said of the DOS pattern in $RbLiZnS_2$, except that it also exhibits noticeable changes due to the replacement of Na with the heavier and larger Rb atom. The upper valence band of the range of −5 eV to 0 eV is still dominated by the S-p orbitals because it is strongly bonded to the atom, and it plays a role in the VBM. Just like $NaLiZnS_2$, the S-s states play a minor role at lower energies. The lower valence band is dominated by Zn-d orbitals and has strong peaks at −6 eV. The intensity and sharpness of Zn-d states in $RbLiZnS_2$ are marginally higher than in $NaLiZnS_2$, suggesting more localized Zn-d behaviour. This could be due to small variations in Zn–S bond lengths or local symmetry generated by the bigger Rb ion. Rb has a significant influence on the conduction band properties. Rb-s, Rb-p and Rb-d orbitals do not contribute much to the valence band but are significant in the conduction band, with a larger contribution especially above 5 eV. The Rb-d states were stretched and added to a larger conduction band by virtue of their higher energy associated with the major quantum number ($n = 4$). The distribution of states in the CB of $RbLiZnS_2$ is denser than in $NaLiZnS_2$, which can have improved carrier transport characteristics when doping or exciting it. The projected density of states (PDOS) reveals a minimal influence of Li-s orbitals on the electronic structure at both valence band maximum (VBM) and conduction band minimum (CBM) states. Na has fewer and more localized s/p orbitals, which contribute at a slightly lower energy in the conduction band, and Rb has larger and more diffuse orbitals, which contribute at a higher energy and over a wider range. The fact that the lack of Rb states near the Fermi level enhances its ionic nature means that it is mostly acting as a charge donor and is not directly taking part in band-edge bonding. This causes the $RbLiZnS_2$ to have a longer conduction band whose properties are more spread out, which may translate to higher optical absorption at the UV-visible regime and potentially a lower effective mass of electrons, which is useful in photovoltaic or thermoelectric device applications. The larger conduction band of $RbLiZnS_2$ could be dielectric responsive and have a better carrier mobility than the well-defined conduction states of $NaLiZnS_2$.

### 3.4 Optical properties

Fig. 5(a) shows the real dielectric function, $\varepsilon_1(\omega)$, which shows the dispersion behaviour of the material, and the ability to slow down light in the structure. $NaLiZnS_2$ and $RbLiZnS_2$ exhibit a systematic increase in $\varepsilon_1(\omega)$ with the photon energy, leading to a sharp increase towards the corresponding maxima between 6–8 eV. The $\varepsilon_1(\omega)$ of $NaLiZnS_2$ is slightly lower than that of $RbLiZnS_2$ in the low-energy regime (below 6.0 e V), implying that it responds poorly to initial polarization. $NaLiZnS_2$ is more efficient than $RbLiZnS_2$, at 7 eV with a peak $\varepsilon_1(\omega)$ exceeding 8.0, as compared with a slightly smaller peak of $\varepsilon_1(\omega)$ of $RbLiZnS_2$. This suggests better electronic polarizability and increased interaction with high-energy photons in $NaLiZnS_2$. Beyond this peak, both materials experience a sharp decline in $\varepsilon_1(\omega)$, transitioning from zero to negative values, indicating entry into a plasma-like regime where the $\varepsilon_1(\omega)$ becomes negative, causing the material to behave like a reflective medium rather than a transparent one. This crossover is associated with the frequency of the plasma, and therefore, the light propagation in the material stops, and the process of reflection prevails. The two have a minor variation in the rate of decrease. The decline and negative values of $RbLiZnS_2$ are lower and slower than those of $NaLiZnS_2$, which means that $RbLiZnS_2$ is more dielectrically stable with increased photon energy. $RbLiZnS_2$ disperses more easily and is more refractive in the far ultraviolet (UV) region, whereas $NaLiZnS_2$ is more polarised in the peak. The variation in $\varepsilon_1(\omega)$ of the two materials can be connected to the variation in the cation size and bonding properties. The larger and less electronegative element Rb has some minimal impact on the electronic structure and density of states, leading to altered optical transitions. Fig. 5(b) shows the imaginary dielectric function $\varepsilon_2(\omega)$, which is the capability of the material to dissipate and absorb energy, mainly due to interband transitions. $NaLiZnS_2$ and $RbLiZnS_2$ possess almost zero values of $\varepsilon_2(\omega)$ and thus are clear in the visible, wide band gaps, so are promising in application in optoelectronics, nonlinear optics and UV devices. At frequencies beyond 4.0 eV, both materials rapidly increase in their $\varepsilon_2(\omega)$ due to the fact that at this energy, photons are energetic enough to initiate electron transfers between the valence and the conduction band. $NaLiZnS_2$ exhibits a peak of a higher value of 9.0 eV, whereas $RbLiZnS_2$ has a smaller value of 8 eV. This indicates that $NaLiZnS_2$ is more

 

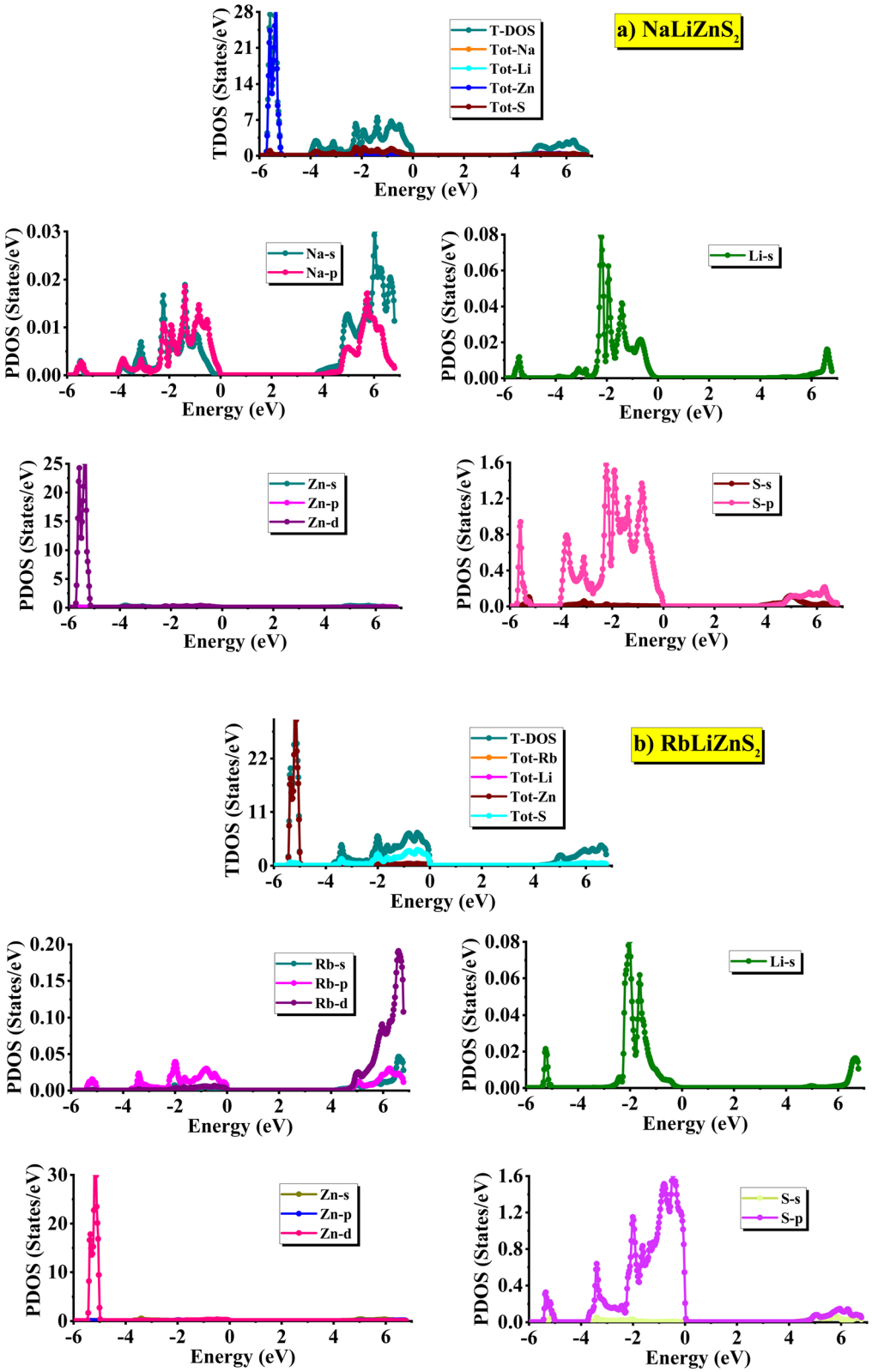


Fig. 4 The calculated density of states of (a) $NaLiZnS_2$ and (b) $RbLiZnS_2$ materials.

inter band transition probability and oscillator strength, and therefore, greater absorption and optical activity in the ultraviolet range compared to $RbLiZnS_2$. This finding indicates that $NaLiZnS_2$ can be more suitable for applications of UV photo detectors and filters that demand a high UV absorbance. After the peak, $\varepsilon_2(\omega)$ of the two materials decreases steadily, which

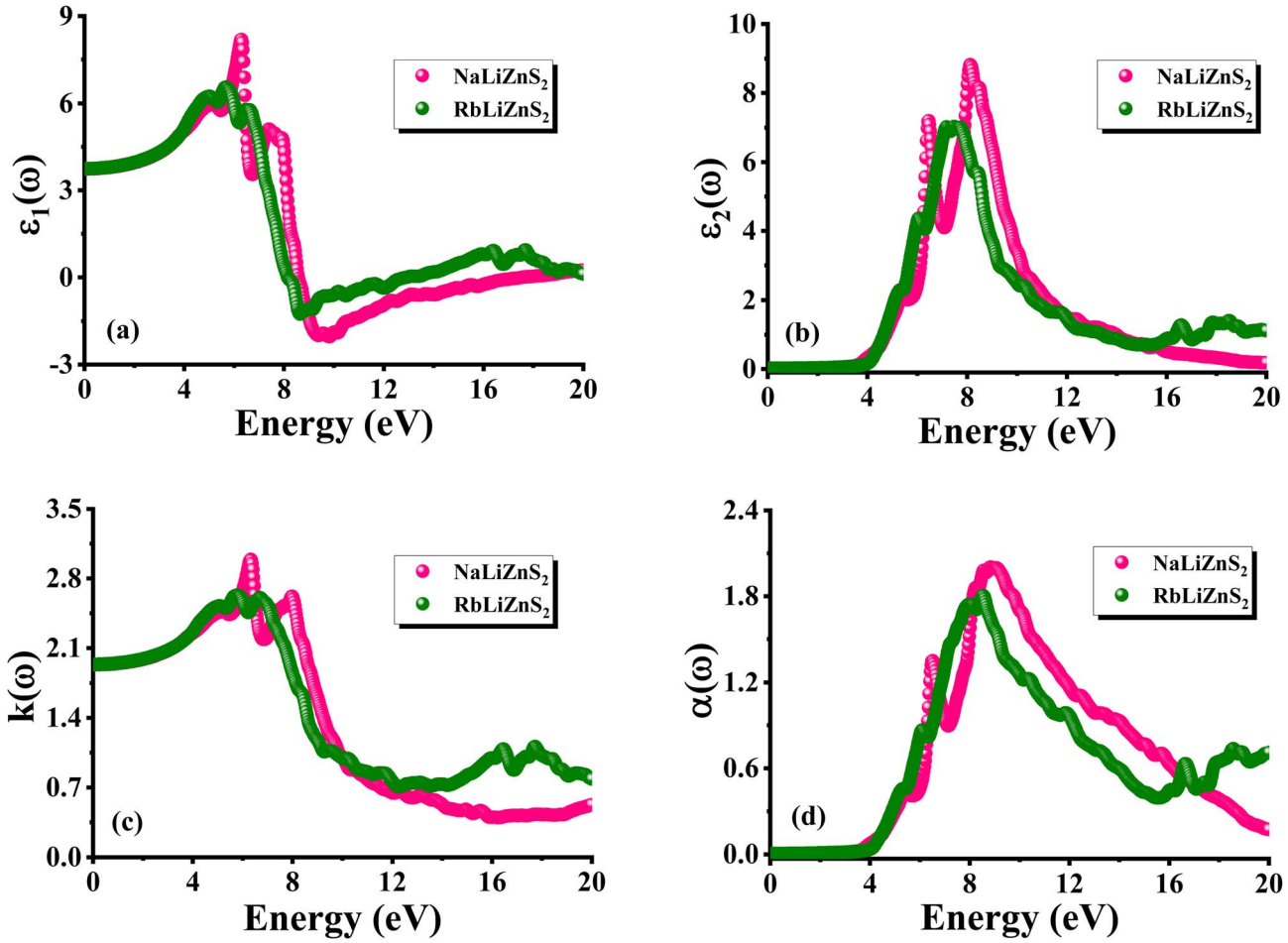


Fig. 5 The calculated (a) real component, (b) imaginary component, (c) extinction coefficient, (d) absorption coefficient, for ALiZnS$_2$ (A = Na, Rb) quaternary chalcogenides.

implies that the transition probability is on the decrease as the photon energy passes beyond the strong absorption region. The RbLiZnS$_2$ shows somewhat higher values of $\varepsilon_2(\omega)$ in the far-UV regime (>12 eV) than NaLiZnS$_2$, which could be due to long-tailed absorption by secondary electronic transitions or defects. It is possible to explain the difference in the $\varepsilon_2(\omega)$ behaviour of the two materials in terms of structural and electronic properties. Na *vs.* Rb has an effect on lattice constants, ionicity and polarizability, which alter electronic band structure and transition probabilities slightly.

The extinction coefficient ($k$), as shown in Fig. 5(c) characterizes the extent of attenuation of light through a substance and is directly proportional to the absorption characteristics. NaLiZnS$_2$ and RbLiZnS$_2$ follow a similar pattern to the $\varepsilon_2(\omega)$ with $k(\omega)$ values near zero in both the infrared and visible spectral ranges, which is indicative of very little absorption and therefore a large band gap and transparency in the visible range. Outside this range, the two materials exhibit a sharp rise in $k(\omega)$, which suggests the onset of significant absorption due to interband electronic transitions. NaLiZnS$_2$ has a higher peak around 3.0, whereas RbLiZnS$_2$ has a somewhat lower peak around 2.6. This means that NaLiZnS$_2$ is more attenuative to light in the ultraviolet (UV) region. NaLiZnS$_2$ possesses a higher absorption efficiency that is capable of finding use in applications associated with UV-like filters, photo detectors, and photovoltaic devices, which demand a powerful light-matter interaction. NaLiZnS$_2$ is better than RbLiZnS$_2$ in terms of peak intensity because of a stronger oscillator and is more likely to undergo electronic transitions. Both materials show a steep decrease in $k$ above 7.3 eV, corresponding to a decrease in absorption when the primary interband transitions are used up. Even though both materials still exhibit similar minor oscillations with increasing photon energy, the influence of attenuation in general reduces significantly. The optical response is mainly fitted within the UV range, with NaLiZnS$_2$ being more efficient in concentrated absorption and energy dissipation. RbLiZnS$_2$ provides a moderate absorption, and this can be useful in applications where a controlled attenuation is required without losing too much energy. Cation substitution (Na *vs.* Rb) is the only slight variation between the two materials that alters the lattice constant, ionicity and density of states, which affect transition probabilities and optical constants. Fig. 5(d) displays the absorption coefficient $\alpha(\omega)$ which is a measure of the amount of light that passes through a material before it is absorbed. NaLiZnS$_2$ and RbLiZnS$_2$ are zero absorption up to 3.6 eV, which means that they are wide band gap

semiconductors and are therefore transparent in the entire visible spectrum. This has rendered them perfect in transparent optical devices such as lenses, coatings and windows to be used in optoelectronics. The sharp increase of both materials occurs beyond 4 eV, and the high absorption is in the ultraviolet (UV) range from 8 to 10 eV. $NaLiZnS_2$ has a slightly higher $\alpha(\omega)$ (approximately 2.0) at these peaks than $RbLiZnS_2$ (1.8) and therefore, better UV absorptiometry. $NaLiZnS_2$ has higher electronic conversion and optical characteristics in the UV region and is suitable for the detection of UV, laser systems, and UV protective coating. On reaching their respective maxima, both materials begin to exhibit a slight decrease in the $\alpha$ value with the increase of photon energy. Nevertheless, absorption does not go to zero in the extreme UV, at 12 eV or more. The remaining absorption may be because of the high-energy transitions or some other secondary processes, including defect state contributions, which indicate that even these materials still have some absorptive properties at very high photon energies. Electronic band structure, transition energies and strength of absorption in $NaLiZnS_2$ and $RbLiZnS_2$ are slightly different since there is a difference in the atomic size and electronegativity.

Fig. 6(a) represents the profile of the optical conductivity $\sigma(\omega)$ of $NaLiZnS_2$ and $RbLiZnS_2$, and shows the interband transition behaviour and electronic structural properties. The conductivity of both materials was found to be very low, nearly zero, up to around 3.7 eV, which shows they have large band gaps and are insulating in the visible region, so they can be used in transparent optical applications. Beyond this point, $\sigma(\omega)$ rapidly rises, reaching approximately 6.7–7.0 eV, which signifies that the interband transitions between the conduction and the valence bands are significant. $NaLiZnS_2$ is a bit higher in its peak conductivity than $RbLiZnS_2$, with a peak conductivity of more than 9000 $cm^{-1}$ at approximately 7.0 eV. This may be because Na has a smaller ionic radius. The difference in size enhances the overlap of orbitals and the strength of the oscillator, resulting in increased optical transitions in $NaLiZnS_2$. The conductivity of the materials beyond the main peak gradually decreases, and significant oscillations occur until the depths of the electronic state (20 eV). Such rhythmic patterns indicate diverse inter band transitions paths with increased photon energy. Fig. 6(b) shows the reflectance $R(\omega)$ of $NaLiZnS_2$ and $RbLiZnS_2$, showing the optical response at different energy levels. The values of the two materials are very low (0.1) in the infrared and visible regions, and this means that these materials are highly transparent and can be used in antireflective coating and optical windows. In the region above 5.0 eV, the reflectance of both materials doubles, indicating the beginning of intense interband electronic transitions in the UV region. $NaLiZnS_2$ has a higher maximum reflectivity of around 0.43 at about 10 eV, as compared to $RbLiZnS_2$, which has a higher reflectivity of about 0.38 at about 8.0 eV, meaning that light-matter interaction is stronger in the UV region with $NaLiZnS_2$. The $NaLiZnS_2$ has a great reflectivity, optical conductivity, and oscillator strength. This is supposedly because the ionic radius of Na is smaller, which allows a lot of orbital hybridization to occur. The smaller cation size in $RbLiZnS_2$ gives it a slightly lower and earlier peak because orbital overlap is less, and the transition energies are changed. Both materials exhibit a gradual decrease in reflectivity above 12 eV, corresponding to decreased interband transition probability with photo-energy increase and a decreased frequency of electronic states available to be excited, therefore reaching their respective maxima. $NaLiZnS_2$ and $RbLiZnS_2$ are also excellent wide-band-gap materials with low reflectivity in the visible and, hence, should be used as transparent optical components. As well, they have large UV reflectivity, which may be used in UV mirrors or protective coatings. The slightly better performance of $NaLiZnS_2$ in the ultraviolet demonstrates its possible superiority in optoelectronic systems where it is important to have better reflectance control at the high-energy photon frequencies.

Fig. 6(c) displays the dependence of the refractive index $n(\omega)$ on photon energy in $NaLiZnS_2$ and $RbLiZnS_2$, which are important insights into the optical response and interaction of light and matter. Starting with a refractive index of approximately 1.8 in the low-energy domain, both materials have their transparency and insulating characteristics at the low photon energies. Energy non-tolerant growth of $n(\omega)$ is fast, with maximum values of $n(\omega)$ at approximately 5.5 eV. $NaLiZnS_2$ has a maximum of approximately 2.8, a little bit less than the $RbLiZnS_2$ at 2.6. $NaLiZnS_2$ is more polarizable than $RbLiZnS_2$, can bend and slow light, and is therefore suited to nonlinear optical and photonic applications. $NaLiZnS_2$ is larger because its Na cations are smaller and thus its orbital overlap and interband transition intensity are high, leading to a high optical density. Beyond 8 eV, $n(\omega)$ falls promptly in both materials, which means that severe interband absorption is beginning and transparency is lost in the deep ultraviolet. This sudden decrease is the place where photon energy is sufficient to excite electrons to higher conduction states, restricting the ability of the material to support coherent optical polarization. $NaLiZnS_2$ has a higher refractive index and a broader range of peaks compared to $RbLiZnS_2$, which makes it better suited for optical applications that require a high level of light confinement and interaction, *e.g.* waveguides, photonic crystals and laser components. The refractive index of $RbLiZnS_2$ is slightly lower and can be used with high optical transparency and stability for applications that require minimal optical distortion. $NaLiZnS_2$ is more refractive in the UV, despite the lower absorption and much higher transparency of both materials in the visible range, so $NaLiZnS_2$ is a better competitor to the next generation optical technologies, which need high polarizability and nonlinear optical phenomena. Fig. 6(d) shows the energy loss function $L(\omega)$ of $NaLiZnS_2$ and $RbLiZnS_2$ that characterizes their plasmonic and electronic excitation processes. Neither material exhibits any energy loss at energies below 8 eV, implying that the incident electrons do not interact with the electronic structure of either material significantly, and their properties as insulators and large band gaps are expected. Beyond this range, $L(\omega)$ soars due to a non-monochromatic collective oscillation of the conduction electrons, *i.e.*, the collective oscillations of the plasma. The $NaLiZnS_2$ dominating plasmon peak is approximately 18 eV, whereas that of $RbLiZnS_2$ is approximately 15 eV. $NaLiZnS_2$ possesses a higher plasma frequency, which means that the density of free electrons is higher and the contribution to

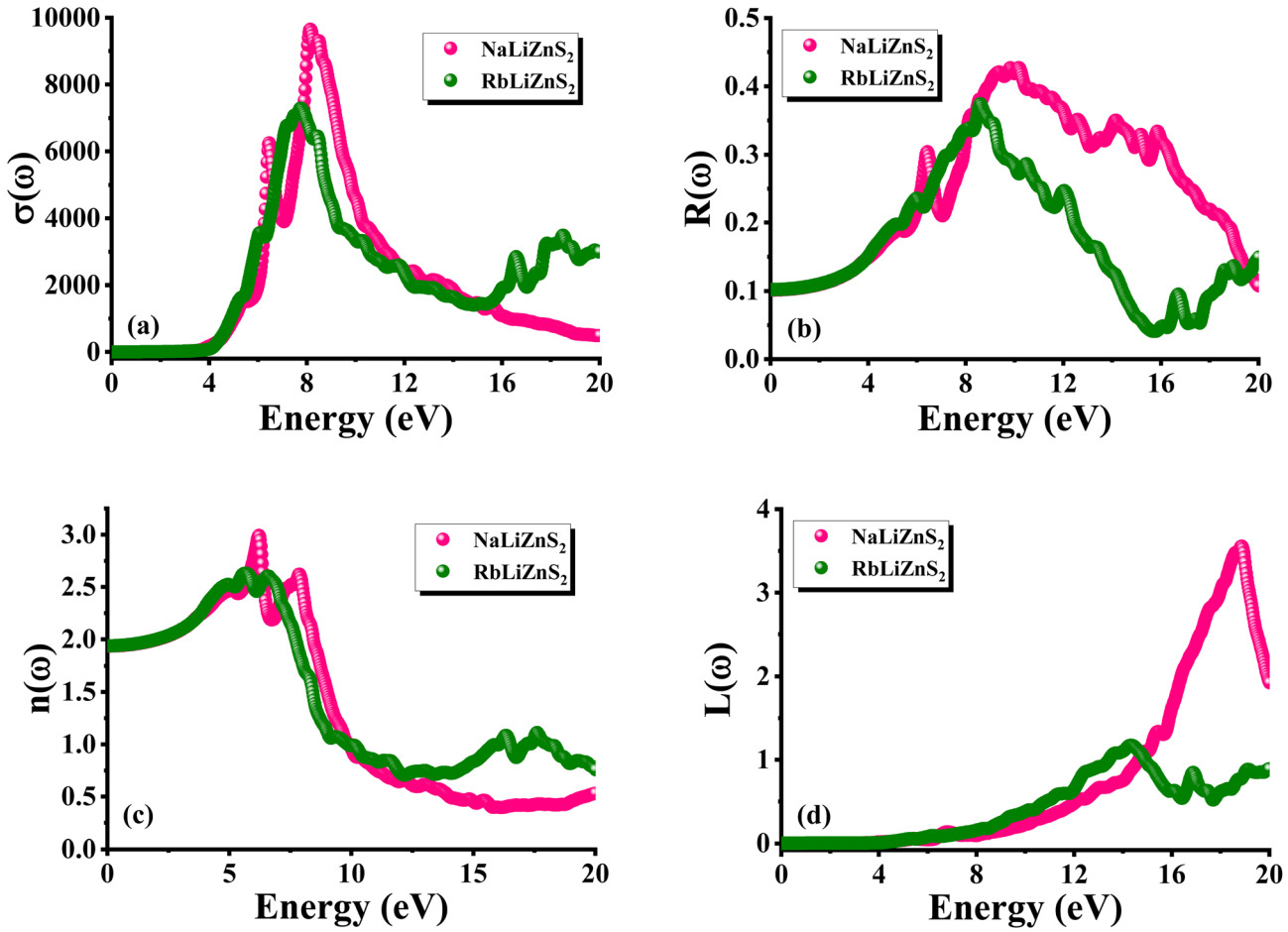


Fig. 6 The calculated (a) optical conductivity, (b) reflectivity, (c) refractive index, and (d) energy loss function for $ALiZnS_2$ (A = Na, Rb) quaternary chalcogenides.

interband transition is more significant in comparison to $RbLiZnS_2$. This may be explained by the fact that the Na cation is smaller, and therefore it increases the orbital overlap and the strength of the electronic interactions. The peaks are associated with the bulk plasmon resonance, which is the maximum electron energy loss, which is important in studying the dielectric behaviour of the material at high frequencies. $NaLiZnS_2$ has a sharper and higher-energy peak, which means that it has a better electromagnetic energy confinement and potential to utilize it in plasmonic and photonic applications. The two materials exhibit a gradual decline in $L(\omega)$ following the initial peaks, indicating reduced energy dissipation in the high photon energies, as there are fewer levels at which the electronic states can be excited. The contrast between the two materials defines the importance of cation size on electronic structure and plasmonic behaviour. $NaLiZnS_2$ proved to be better in regard to higher plasmon frequency and enhanced interband effects.

### 3.5 Thermoelectric properties

The thermoelectric transport properties of the quaternary chalcogenides of $NaLiZnS_2$ and $RbLiZnS_2$, as illustrated in Fig. 7(a–f), exhibit varying temperature-dependent behaviours and material-dependent variations that determine the possible efficiency of their usage in the thermoelectric field. The inherent limitations in the thermoelectric theory used were that the transport behaviour is assumed under the constant relaxation time approximation, which fails to consider complicated scattering processes like those from defects, grain boundaries, and anharmonic phonons. Fig. 7(a) shows that the electronic thermal conductivity of $NaLiZnS_2$ and $RbLiZnS_2$ is nearly linear with temperature. This is attributed to the amplified temperature-dependent charge carrier energy and other related scattering processes. This trend is an expression of the reality that at high temperatures, carriers are better endowed with kinetic energy, and that they are better contributors to thermal transport, all of which is a basic understanding of thermoelectric transport theory. The $RbLiZnS_2$ is better than the $NaLiZnS_2$ at high temperatures, although both materials progress on a monotonic trend as the temperature increases. The difference is directly associated with its higher electrical conductivity, as seen in Fig. 7(b). It may be justified using the Wiedemann–Franz equation, which stipulates that $\kappa_e$ is proportional to $\sigma$ *via* the Lorenz number. An increase in $\sigma$ causes an increase in $\kappa_e$ at the same carrier scattering regimes. $RbLiZnS_2$ possesses a slightly larger kappa/s where the carrier scattering is lesser, or the density of state around the Fermi level is denser, leading to

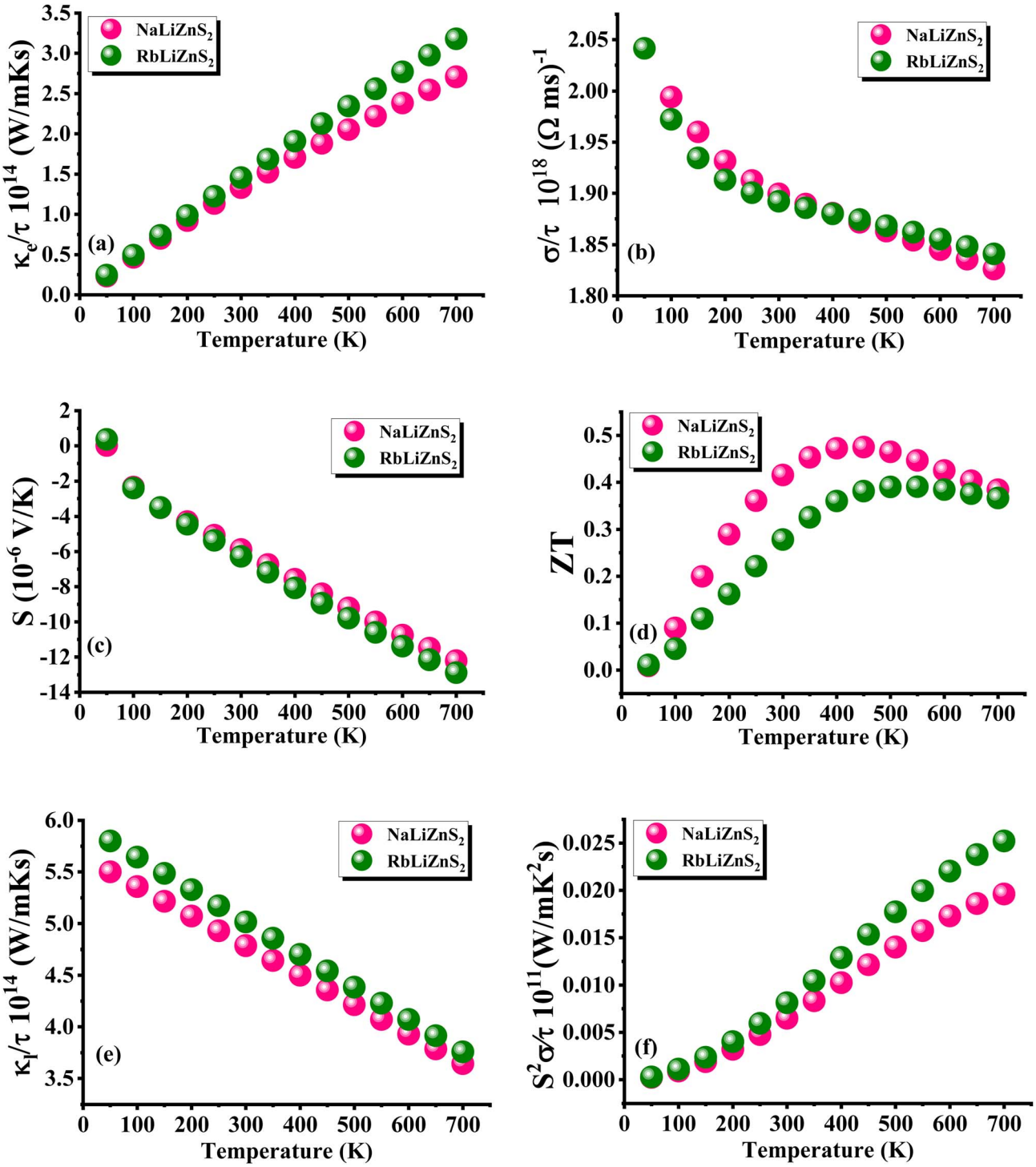


Fig. 7 The calculated (a) electronic thermal conductivity, (b) electrical conductivity, (c) seebeck coefficient, (d) figure of merit, (e) lattice thermal conductivity, and (f) power factor for $ALiZnS_2$ (A = Na, Rb) quaternary chalcogenides.

an increase in carrier mobility as well as heat transportation. Greater $\kappa_e$ tends to enhance overall thermal conductivity ($\kappa$), and hence decrease the figure of merit ($ZT$) in thermoelectric applications, although the difference between them is relatively small. This indicates that the contribution of $\kappa_e$ to the total $\kappa_e$ will be comparatively small compared to the thermal conductivity of the lattice in these wide-band gap chalcogenides, which are quaternary. Moreover, the almost parallel gradients of $\kappa$ *vs.* temperature curves of the two materials indicate that the same dominating scattering mechanisms, which would be due to acoustic phonon interactions and not ionised impurity scattering, do occur in both cases, giving

different temperature dependencies. The noted linearity also suggests that bipolar thermal conduction by minority carriers cannot be important in the temperature regime under study, which is consistent with their semiconducting character and with their band gaps that are large enough. Fig. 7(b) demonstrates that the electrical conductivity per relaxation time ($\sigma/t$) of both $NaLiZnS_2$ and $RbLiZnS_2$ exhibits a definite tendency with increasing temperature, and this is a typical feature of the metallic or degenerate semiconductor behaviour. An increase in temperature increases phonon–electron scattering, and carrier mobility decreases. The dependence of the ratio of $\sigma/\tau$ to temperature indicates that both compounds operate in a regime where thermally activated scattering processes play a significant role instead of carrier excitation across the band gap, which is in line with their relatively large initial values of $\sigma/\tau$. $RbLiZnS_2$ regularly wins the race in terms of $\sigma/T$ over $NaLiZnS_2$, especially at low temperatures, where phonon scattering is weaker, and carrier mobility has a greater contribution to the conductivity. One of the strengths of $RbLiZnS_2$ is its lower effective mass, which enables it to achieve higher carrier velocities and possibly carrier concentration. These aspects enhance efficiency in the transmission of electricity. $RbLiZnS_2$ has a higher electronic thermal conductivity ($\kappa_e$) because it has a higher sigma/tau (Fig. 7(a)). This would be in line with the Wiedemann–Franz equation that connects thermal and electrical transport, by both sharing a common carrier population. The benefit of higher $\sigma/\tau$ values in thermoelectric activity is their direct positive effect on the power factor ($S^2\sigma$). They, however, also increase $\kappa\,\varepsilon$, which is counterproductive to the figure of merit ($ZT$) without an adequate countermeasure of low lattice thermal conductivity. The fact that the slope of $1/\tau$ of both materials decreases rapidly with temperature shows that temperature dependence is reduced to phonon scattering at high temperatures, and impurity or defect scattering is not relevant. $RbLiZnS_2$ has consistently greater $\sigma/\tau$, suggesting that its conduction band structure and density of states may be more advantageous for carrier mobility compared to $NaLiZnS_2$. This could be owing to changes in atomic mass, bonding strength, or crystal symmetry between Rb- and Na-based systems.

Fig. 7(c) indicates that the Seebeck coefficient ($S$) of $NaLiZnS_2$ and $RbLiZnS_2$ exhibits an inverse relationship with the temperature, *i.e.* decreasing gradually between low temperature and high temperature. Such a negative slope is typical of degenerate or highly doped semiconductors, where carrier diffusion predominates the thermoelectric response. Through an increase in temperature, thermal excitation of carriers leads to a decrease in the asymmetry in the energy distribution of charge carriers relative to the Fermi level, a decrease in $S$. The reduction in energy-dependent carrier transport efficiency is a reason why $S$ of both materials kept on decreasing steadily. $NaLiZnS_2$ in the entire range studied is consistently found to have a somewhat higher value of $S$ than $RbLiZnS_2$. This indicates that although $RbLiZnS_2$ has a higher electrical conductivity, its higher carrier concentration probably causes $S$ to be lower because the carrier density and Seebeck coefficient have an inverse relationship as described by the Pisarenko equation. $NaLiZnS_2$ has a lower carrier concentration, hence a higher thermoelectric voltage divided by unit temperature difference. The trade-off between larger $\sigma$ and smaller $S$ in $RbLiZnS_2$ and smaller $\sigma$ and larger $S$ in $NaLiZnS_2$ is a typical trade-off in the optimisation of the thermoelectric materials, because both are important variables in the power factor ($S^2\sigma$). The in general parallel temperature-dependent trends of the two materials indicate that these materials share the same scattering mechanisms, which is likely to be dominated by acoustic phonon scattering, and bipolar conduction effects are also negligible in the examined range, which is reasonable as long as the band gaps are large enough. The slightly larger $S$ in $NaLiZnS_2$ can perhaps be associated with changes in electronic band structure, perhaps through an increase in effective mass or more salient density-of-states properties associated with the Fermi level, which enhances thermopower. This benefit in $S$ should, however, be considered based on the total thermoelectric performance. $NaLiZnS_2$ generates a higher voltage per degree of temperature difference, although $RbLiZnS_2$ has a better electrical conductivity, which allows conductivity to flow, and thus it may give a higher power factor when the difference in $S$ is not too great. Fig. 7(d) illustrates that the temperature of the thermoelectric figure of merit ($ZT$) of both $NaLiZnS_2$ and $RbLiZnS_2$ exhibits non-monotonic behaviour in the two materials. $ZT$ increases gradually at low temperatures and then progressively at higher temperatures, showing that $ZT$ reaches an optimal range of 400–500 K, beyond which the negative influences of increased electronic thermal conductivity ($\kappa$) and reduced $S$ by increased bipolar conduction or increased carrier dispersion overshadow the benefits of $\sigma$. $NaLiZnS_2$ has a higher $ZT$ of 0.46 than 0.38 of $RbLiZnS_2$ which shows a superior thermoelectric balance. Although $RbLiZnS_2$ exhibits a slightly higher electrical conductivity ($\sigma$), $NaLiZnS_2$ compensates with a marginally larger Seebeck coefficient ($S$), which enhances the power factor ($S^2\sigma$). More importantly, $NaLiZnS_2$ shows significantly reduced electronic ($\kappa_e$) and lattice ($\kappa_l$) thermal conductivities, leading to lower total thermal conductivity ($\kappa$), thereby minimizing heat loss and improving thermoelectric energy conversion efficiency. This combination results in an improved power factor of $NaLiZnS_2$, especially as the temperature gets higher to its maximum working temperature and its electronic and phononic transport characteristics are maximized. The importance of the thermal transport advantage is that $\kappa$ can be a more useful measure of phonon scattering by mass or bond disorder. Fig. 7(e) illustrates that both lattice thermal conductivity per relaxation time for $NaLiZnS_2$ and $RbLiZnS_2$ have a negative dependence on temperature. This is explained by the fact that the phonon–phonon Umklapp scattering rises as the thermal energy is high. The sluggishness of this thermal dependence is possible because the greater the thermal vibrations, the greater the probability of phonon collision that eliminates the heat-carrying modes and thus inhibits thermal transport of lattices.

At any given temperature, $RbLiZnS_2$ exhibits higher $\kappa_e/\tau$ values than $NaLiZnS_2$, indicating a lower phonon scattering. This is due to the fact that the two materials differ in their crystal structure, distribution of atomic mass and bonding properties. $NaLiZnS_2$ can also have higher atomic mass contrast

 

effects and distortion of the lattice, leading to more phonon scattering centres and shorter mean free paths. $NaLiZnS_2$ is structurally stiff, and its average mass is greater than that of $RbLiZnS_2$, which disrupts the coherent phonon transfer, much more reducing $\kappa_e$ than in $RbLiZnS_2$, where phonon movement does not appear to be inhibited. Lower lattice thermal conductivity in thermoelectric performance decreases overall thermal conductivity and increases the figure of merit ($ZT$) at comparable electrical qualities. $NaLiZnS_2$ has a lower $\kappa$, which is the best thermoelectric material as it increases the heat-to-electric conversion efficiency, yet leaves electrical transport unaffected. The fact that both materials have decreasing slopes of $\kappa$ is evidence that the same phonon scattering process persists, that is, that of Umklapp processes. $NaLiZnS_2$, on the other hand, shows a steady suppression behaviour at all temperatures, indicating the usefulness of the intrinsic phonon scattering centres. Microstructural parameters like anharmonicity of lattice and point-defect dislocations can play a more significant role in $NaLiZnS_2$. Fig. 7(f) displays the power factor of $NaLiZnS_2$ and $RbLiZnS_2$, and the trend is clearly toward increasing with temperature, which suggests a combination of the Seebeck coefficient ($S$) and electrical conductivity ($S$). Even though the trend in both materials is increasing, $RbLiZnS_2$ has a higher tendency to generate higher power factor values in all temperatures. This supremacy is mostly due to its much higher $\sigma$, which more than compensates for its somewhat lower $S$ relative to $NaLiZnS_2$. $RbLiZnS_2$ maintains an advantage despite a disadvantage in $S$. This illustrates the larger weighting of $\sigma$ in determining the power factor when the difference in $S$ is moderate, as $S^2\sigma$ amplifies small fluctuations but cannot offset a big conductivity disparity. The increasing trend with temperature shows that, for both materials, the minor drop in S is exceeded by the temperature-driven enhancement in $\sigma/\tau$ contribution to $S^2\sigma/\tau$. This could be due to changes in carrier scattering dynamics at elevated thermal energy. $RbLiZnS_2$ may be more suited for thermoelectric systems that prioritize optimizing electrical output per unit temperature difference, particularly when heat dissipation is minimal or external cooling is provided.

## 4 Conclusions

This first-principles work describes how alkali-metal substitution affects the multifunctional properties of $ALiZnS_2$ (A = Na, Rb) quaternary sulfides optimized in the tetragonal structure with $I4m2$ space group. The bigger $Rb^+$ ion enhances equilibrium volume, reduces bonding rigidity and enhances compressibility. Both compounds are stable at equilibrium with both energy and mechanical stability. Elastic analysis can be used to explain this difference quantitatively: $NaLiZnS_2$ is larger in bulk, shear, and Young's moduli, indicating that it is better in stiffness and resistant to deformation. $RbLiZnS_2$ exhibits greater Cauchy pressure and Pugh ratio, indicating a better bond of ion and ductile property. The two materials are moderately anisotropic elastics and represent all the Born stability criteria. The calculations of electronic structures prove that both systems have direct wide-band-gap semiconductors, and the TB-mBJ gaps of 3.43 eV in $NaLiZnS_2$ and 4.04 eV in $RbLiZnS_2$. S-p states dominate the valence band, and localized Zn-d states are at higher energies, and localized Zn-s/p states form the conduction band. Rb replacement increases the conduction channel and increases the band separation, which enhances electrical stability and UV transparency. $NaLiZnS_2$ has increased dielectric peaks, optic index, optical conductivity, and plasma frequency, indicating an intense interaction between light and matter. Through optical response analysis, there were no significant absorption and reflectivity values in the visible range, sharp edges of absorption in the ultraviolet and clear interband transitions between 6–10 eV. The thermoelectric transport data have the monotonic decrease of electrical conductivity and Seebeck coefficient with temperature, the monotonic decrease of lattice thermal conductivity by Umklapp scattering, and the definite positive performance advantage of $NaLiZnS_2$, which remains higher at peak $ZT$ ($\sim$0.46) than $RbLiZnS_2$. In general, the findings reveal that the tuned alkali-metal substitution is an influential method of controlling mechanical durability, electronic gaps, optical activities and thermoelectric efficacy in quaternary sulfide semiconductors.

## Conflicts of interest

The authors declare no conflicts of interest.

## Data availability

Data are available upon request from the corresponding author.

## Acknowledgements

This work was supported and funded by the Deanship of Scientific Research at Imam Mohammad Ibn Saud Islamic University (IMSIU) (grant number IMSIU-DDRSP2603).

## References

1 X. Huang, S. H. Yang, W. Liu and S. P. Guo, *Inorg. Chem.*, 2022, **61**, 12954–12958.
2 M. M. Chen, H. G. Xue and S. P. Guo, *Coord. Chem. Rev.*, 2018, **368**, 115–133.
3 W. Zhou, W. D. Yao, R. L. Tang, H. Xue and S. P. Guo, *J. Alloys Compd.*, 2021, **867**, 158879.
4 Y. Chi, T. F. Jiang, H. G. Xue and S. P. Guo, *Inorg. Chem.*, 2019, **58**, 3574–3577.
5 G. Yang, L.-H. Li, C. Wu, M. G. Humphrey and C. Zhang, *Inorg. Chem.*, 2019, **58**, 12582–12589.
6 Y. Li, X. Song, Y. Zhong, Y. Guo, M. Ji, Z. You and Y. An, *J. Alloys Compd.*, 2021, **872**, 159591.
7 W. Zhou, Q. Zhang, W.-D. Yao, H. Xue and S.-P. Guo, *Inorg. Chem.*, 2021, **60**, 12536–12544.
8 Y. Xiao, M.-M. Chen, Y.-Y. Shen, P.-F. Liu, H. Lin and Y. Liu, *Inorg. Chem. Front.*, 2021, **8**, 2835–2843.
9 G. Shan and S. Bao, *Phys. E*, 2006, **35**, 161–167.

10 J. Guo, S. Jin, G. Wang, S. Wang, K. Zhu, T. Zhou, M. He and X. Chen, *Phys. Rev. B: Condens. Matter Mater. Phys.*, 2010, **82**, 180520.
11 A. F. Wang, J. J. Ying, Y. J. Yan, R. H. Liu, X. G. Luo, Z. Y. Li, X. F. Wang, M. Zhang, G. J. Ye, P. Cheng, Z. J. Xiang and X. H. Chen, *Phys. Rev. B: Condens. Matter Mater. Phys.*, 2011, **83**, 060512.
12 Z. W. Wang, Z. Wang, Y. J. Song, C. Ma, Y. Cai, Z. Chen, H. F. Tian, H. X. Yang, G. F. Chen and J. Q. Li, *J. Phys. Chem. C*, 2012, **116**, 17847–17852.
13 J. J. Ying, Z. J. Xiang, Z. Y. Li, Y. J. Yan, M. Zhang, A. F. Wang, X. G. Luo and X. H. Chen, *Phys. Rev. B: Condens. Matter Mater. Phys.*, 2012, **85**, 054506.
14 X. Lai, H. Zhang, Y. Wang, X. Wang, X. Zhang, J. Lin and F. Huang, *J. Am. Chem. Soc.*, 2015, **137**, 10148–10151.
15 B. Wang, Z. Guo, F. Sun, J. Deng, J. Lin, D. Wu and W. Yuan, *J. Solid State Chem.*, 2019, **272**, 126–130.
16 D. Yuan, N. Liu, K. Li, S. Jin, J. Guo and X. Chen, *Inorg. Chem.*, 2017, **56**, 13187–13193.
17 S. Alagarsamy, K. Balakrishnan and P. Vajeeston, *ACS Omega*, 2025, **10**, 49924–49940.
18 R. Fong, J. R. Dahn, R. J. Batchelor, F. W. B. Einstein and C. H. W. Jones, *Phys. Rev. B: Condens. Matter Mater. Phys.*, 1989, **39**, 4424.
19 J. Llanos, P. Valenzuela, C. Mujica, A. Buljan and R. Ramirez, *J. Solid State Chem.*, 1996, **122**, 31–35.
20 R. J. Batchelor, F. W. B. Einstein, C. H. W. Jones, R. Fong and J. R. Dahn, *Phys. Rev. B: Condens. Matter Mater. Phys.*, 1988, **37**, 3699.
21 M. Oledzka, K. V. Ramanujachary and M. Greenblatt, *Mater. Res. Bull.*, 1996, **31**, 1491–1497.
22 M. Oledzka, C. L. Lee, K. V. Ramanujachary and M. Greenblatt, *Mater. Res. Bull.*, 1997, **32**, 889–895.
23 W. M. Kacholovskaya, B. S. Osipov, N. G. Nazarenko, W. A. Kykoyev, A. O. Mazmanian, I. N. Yegorov and L. N. Kaplunnik, *Zap. Vsesoyuznogo Mineral. Obshchestva*, 1988, **117**, 204.
24 M. Oledzka, K. V. Ramanujachary and M. Greenblatt, *Chem. Mater.*, 1998, **10**, 322–328.
25 A. Virtue, X. Zhou, B. Wilfong, J. W. Lynn, K. Taddei, P. Zavalij, L. Wang and E. E. Rodriguez, *Phys. Rev. Mater.*, 2019, **3**, 044411.
26 Y. Ren, X. Lai, M. Guo, R. Wang, J. Deng and J. Jian, *J. Alloys Compd.*, 2020, **822**, 153613.
27 L. Zhou, L. Kou, Y. Sun, C. Felser, F. Hu, G. Shan, S. C. Smith, B. Yan and T. Frauenheim, *Nano Lett.*, 2015, **15**, 7867–7872.
28 S.-C. Wu, G. Shan and B. Yan, *Phys. Rev. Lett.*, 2014, **113**, 256401.
29 G. Kreiner, A. Kalache, S. Hausdorf, V. Alijani, J. Qian, G. Shan, U. Burkhardt, S. Ouardi and C. Felser, *Z. Anorg. Allg. Chem.*, 2014, **640**, 738–752.
30 Y. Liu, Y. Li, Y. Guo, Y. Sun, X. Cao, M. Ji, Z. You and Y. An, *J. Alloys Compd.*, 2020, **847**, 156450.
31 B. Denga, G. H. Chana, F. Q. Huangb, D. L. Graya, D. E. Ellisa, R. P. V. Duynea and J. A. Ibers, *J. Solid State Chem.*, 2007, **180**, 759–764.
32 J. P. Perdew, K. Burke and M. Ernzerhof, *Phys. Rev. Lett.*, 1996, **77**, 3865–3868.
33 F. Tran, P. Blaha and K. Schwarz, *J. Phys.:Condens. Matter*, 2007, **19**, 196208.
34 P. Blaha, K. Schwarz, F. Tran, R. Laskowski, G. K. H. Madsen and L. D. Marks, *J. Chem. Phys.*, 2020, **152**, 074101.
35 Q. Yang, Y. Li, C. Felser and B. Yan, *Newton*, 2025, **1**, 100015.